



HAL
open science

Stereolithography coupled with spark plasma sintering to produce Ti-6Al-4V complex shapes

Joseph Le Cloarec, Sylvain Marinel, Claude Estournès, Moukrane Dehmas,
Cendrine Folton, Charles Manière

► **To cite this version:**

Joseph Le Cloarec, Sylvain Marinel, Claude Estournès, Moukrane Dehmas, Cendrine Folton, et al.. Stereolithography coupled with spark plasma sintering to produce Ti-6Al-4V complex shapes. *Journal of Manufacturing Processes*, 2024, 114, pp.122-135. 10.1016/j.jmapro.2024.01.084 . hal-04532046

HAL Id: hal-04532046

<https://hal.science/hal-04532046v1>

Submitted on 4 Apr 2024

HAL is a multi-disciplinary open access archive for the deposit and dissemination of scientific research documents, whether they are published or not. The documents may come from teaching and research institutions in France or abroad, or from public or private research centers.

L'archive ouverte pluridisciplinaire **HAL**, est destinée au dépôt et à la diffusion de documents scientifiques de niveau recherche, publiés ou non, émanant des établissements d'enseignement et de recherche français ou étrangers, des laboratoires publics ou privés.

Stereolithography coupled with spark plasma sintering to produce Ti-6Al-4V complex shapes

Joseph Le Cloarec^{1,2*}, Sylvain Marinel¹, Claude Estournès², Moukrane Dehmas³, Cendrine Folton¹, Charles Manière^{1*}.

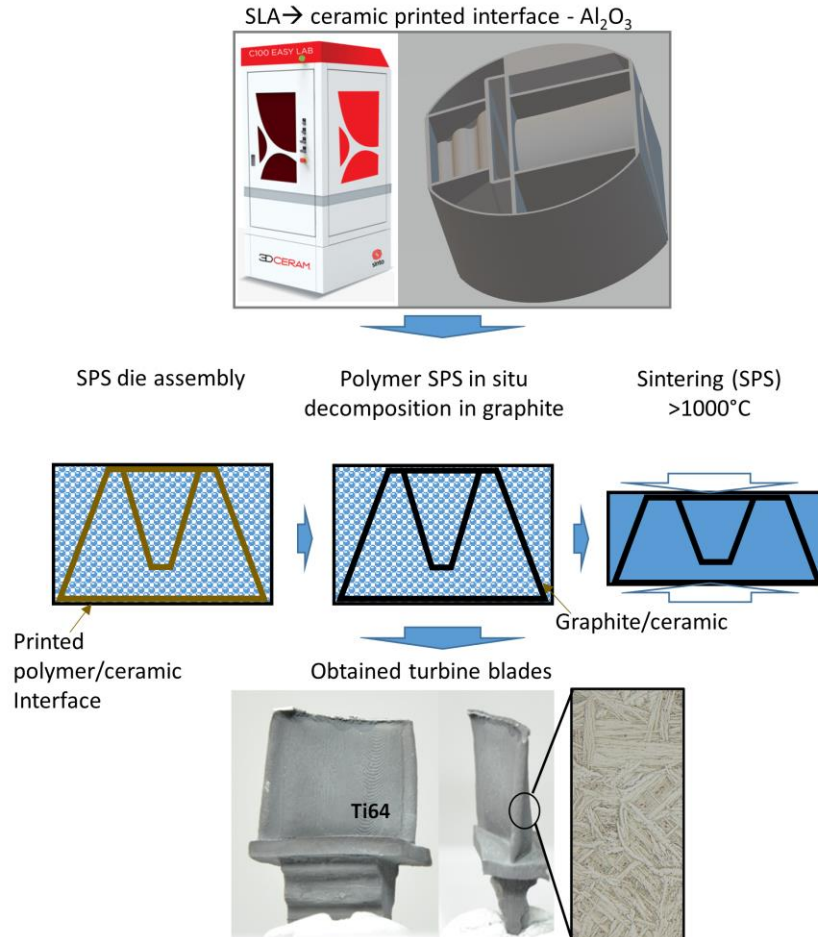
1. CRISMAT, Normandie Univ, ENSICAEN, UNICAEN, CNRS, 14000, Caen, France
2. CIRIMAT, Université Toulouse 3 Paul Sabatier, Toulouse INP, CNRS, Université de Toulouse, 118 Route de Narbonne, 31062 Toulouse cedex 9 - France
3. CIRIMAT, Toulouse INP, Université Toulouse 3 Paul Sabatier, CNRS, Université de Toulouse, 4 allée Emile Monso - BP44362, 31030 Toulouse cedex 4 - France

Keywords

Spark Plasma Sintering; stereolithography; sintering parameters; sintering simulation; Ti-6Al-4V;

Abstract:

Coupling ceramic stereolithography (SLA) and spark plasma sintering (SPS) is possible by the deformed interface approach. Such innovative approach enables the production of highly complex shapes through the high resolution of SLA and the highly controllable microstructures of SPS. This process circumvents at the same time the complex thermal history of other additive manufacturing methods like selective laser melting (SLM) and all issues of complex shapes production in pressing devices like SPS. The production of Ti-6Al-4V thick conical shape and thin complex turbine blade shape is presented in this article. The powder and interface co-sintering requires a finite element (FEM) simulation tool to predict the Ti-6Al-4V high temperature sintering and the impact of the interface on the shape distortions. The sintering mechanisms, microstructures, and mechanical properties were characterized for all the shapes. This work shows the prototyping of titanium complex parts by SLA coupled to SPS is on the verge to become possible.



* Corresponding authors:

Laboratoire de cristallographie et sciences des matériaux (CRISMAT)

6 Bvd du maréchal Juin 14050 CAEN CEDEX 4, France

E-mail address: joseph.le-cloarec@ensicaen.fr; charles.maniere@ensicaen.fr

Nomenclature and abbreviations

θ Porosity

$\dot{\theta}$ Porosity elimination rate (s^{-1})

$\underline{\sigma}$ Stress tensor ($N.m^{-2}$)

σ_{eq} Equivalent stress ($N.m^{-2}$)

$\underline{\dot{\epsilon}}$ Strain rate tensor (s^{-1})

n Creep law stress exponent

A_0 Deformability pre-exponential factor ($Ks^{-1}Pa^{-n}$)

Q Deformability activation energy ($J.mol^{-1}$)

T Temperature (K)

φ Shear modulus

ψ Bulk modulus

$\dot{\epsilon}_z$ Axial strain rate tensor component (s^{-1})

σ_z Axial stress tensor component ($N.m^{-2}$)

θ_{cf} Critical final porosity

SPS Spark Plasma Sintering

HP hot pressing

HIP hot isostatic pressing

1. Introduction

Spark plasma sintering (SPS) die pressing is not well suited to the fabrication of 3D complex shapes materials. They can be produced using multiple punches [1] but like in powder metallurgy [2], differential punches motions are required to ensure full densification, which is difficult by SPS. Consequently, sacrificial powder is used to control the motion of punches [3] or internal interface [4] that allows to sinter complex shapes. This last interface method allows to couple different 3D printing approaches with SPS [5]. Submold 3D polymer/ceramic interface can be 3D printed, then filled with powder and partially graded into graphite or

graphite/ceramic interfaces that follows the sintering of the powder and allows post-SPS ejection of the internal complex shape [6].

This method is particularly efficient for metals & alloys and the interface may imply some deformation that needs to be anticipated by simulation. In this article, alumina stereolithography is used to 3D print interface and fabricate Ti-6Al-4V shapes by SPS from gas atomized powder. The aim of the study is to simulate shape evolution during the SPS test.

Gas atomized metals and alloys particles are generally large in size (from 0.01-1mm) and with very spherical shape [7–9]. After sieving, nearly monodisperse powder with high fluidity can be obtained. Such powders are very interesting for metal additive manufacturing [10,11] where successive layer of powders needs to be deposited. Their fluidity is also very interesting for the loading of metallic powders in various molds like for injection molding [12], HIP [13], hot forming [14] and for the submold methods [4,5,15] developed to produce complex shapes by HP or SPS. In these methods, simulating the high temperature and high pressure densification of the metallic powder is of great interest to predict porosity gradients or distortions of the shapes during the sintering and to anticipate corrective machining in specific zones of the parts [16–18]. SPS of metals and alloys involves different phenomena such as the deformation of the particles, their rearrangement, eventual phase transition, grain growth, capillarity forces if the particles are small and very different sintering behavior depending on the atmosphere [7,19]. SPS of metal powder is conducted in vacuum, inert or reductive atmosphere to avoid the oxidation of the particle surface [9,20]. In general, the sintering is dominated by a hot deformation of metallic particles by creep mechanisms. Gas atomized powders are large in size and well arranged, which implicate the capillarity forces are negligible against the applied stress and the initial compaction is high. The sintering can be modeled by a porous viscoplastic model originated from the continuum theory of sintering [21,22].

The assessment of the sintering model parameters can be a very difficult task requiring determining the high temperature creep behavior of the metal and the shear and bulk moduli reflecting densification behavior [23,24]. The first groups of parameters represent the

temperature dependence and the model stress sensitivity while the second group represents porosity dependent terms. The assessment of these parameters requires a long study involving high temperature mechanical tests with fully dense and porous specimens [25–28]. It is possible to greatly simplify this long identification study by using theoretical hypotheses on the shear and bulk moduli and identify the sintering by direct linear regression [18,29].

In this study, the direct regression approach [18,29] applied to the spark plasma sintering at different heating rates are used with a Ti-6Al-4V alloy powder. Using stepwise SPS experimental tests, the stress exponent “ n ” (a value indicating the sintering mechanism) is identified [30]. Considering this “ n ” value, a linear regression on several sintering tests with different heating rates allows to determine the creep parameters and porosity dependent moduli from Skorohod theoretical base [31]. With this method, a predictive simulating model of Ti-6Al-4V sintering has been established. This sintering model is then used to reveal defects on Ti-6Al-4V parts produced by a complex shape sintering method in SPS that we develop.

2. Theory and calculation

2.1. Model description

The continuum theory of sintering [21] defines the sintering behavior by the following equation that neglects the capillarity forces.

$$\underline{\sigma} = \frac{\sigma_{eq}}{\dot{\epsilon}_{eq}} \left(\varphi \underline{\dot{\epsilon}} + \left(\psi - \frac{1}{3} \varphi \right) \dot{\epsilon} \mathbf{i} \right) \quad (1)$$

The equivalent stress and strain rate ratio are defined by the creep behavior of the metal (see equation below) with A_0 , Q , and n , the unknown parameters to be refined.

$$\dot{\epsilon}_{eq} = A_0 \frac{\exp\left(\frac{-Q}{RT}\right)}{T} \sigma_{eq}^n \quad (2)$$

The equivalent stress and strain rate tensors neglecting the capillarity forces are defined by:

$$\sigma_{eq} = \frac{\sqrt{\frac{\tau^2 + p^2}{\varphi + \psi}}}{\sqrt{1-\theta}} \quad (3)$$

$$\dot{\epsilon}_{eq} = \frac{1}{\sqrt{1-\theta}} \sqrt{\varphi \dot{\gamma}^2 + \psi \dot{\epsilon}^2} \quad (4)$$

Where φ and ψ are porosity functions to be determined experimentally. The stress and strain rate invariants are defined by:

$$\tau = \frac{\sqrt{(\sigma_x - \sigma_y)^2 + (\sigma_y - \sigma_z)^2 + (\sigma_z - \sigma_x)^2 + 6(\sigma_{xy}^2 + \sigma_{yz}^2 + \sigma_{xz}^2)}}{\sqrt{3}} \quad (5)$$

$$P = \frac{\sigma_x + \sigma_y + \sigma_z}{3} = \frac{l_1}{3} \quad (6)$$

$$\dot{\gamma} = \sqrt{2(\dot{\varepsilon}_{xy}^2 + \dot{\varepsilon}_{xz}^2 + \dot{\varepsilon}_{yz}^2) + \frac{2}{3}(\dot{\varepsilon}_x^2 + \dot{\varepsilon}_y^2 + \dot{\varepsilon}_z^2) - \frac{2}{3}(\dot{\varepsilon}_x \dot{\varepsilon}_y + \dot{\varepsilon}_x \dot{\varepsilon}_z + \dot{\varepsilon}_y \dot{\varepsilon}_z)} \quad (7)$$

$$\dot{\varepsilon} = \dot{\varepsilon}_x + \dot{\varepsilon}_y + \dot{\varepsilon}_z \quad (8)$$

Finally, the mass conservation is used to link the rate of porosity elimination and the volume change rate.

$$\frac{\dot{\theta}}{(1-\theta)} = \dot{\varepsilon} \quad (9)$$

Above group of equations can simulate pressure assisted sintering of different complex configurations. In hot pressing or spark plasma sintering, if friction or thermal gradients are neglected, this complex group of equations can be simplified in a simple analytic equation, which is particularly interesting to determine the sintering parameters. The analytic equation of spark plasma sintering neglecting the capillarity forces is the following [23]:

$$|\dot{\varepsilon}_z| = \left| \frac{\dot{\theta}}{(1-\theta)} \right| = A_0 \frac{\exp\left(\frac{-Q}{RT}\right)}{T} \left(\psi + \frac{2}{3}\varphi \right)^{\frac{-n-1}{2}} (1-\theta)^{\frac{1-n}{2}} |\sigma_z|^n \quad (10)$$

2.2. Determination of stress exponent n

For two die compaction tests at the same T , θ and at different applied stress (σ_z), we obtain:

$$\left| \frac{\dot{\theta}_1}{\dot{\theta}_2} \right| = \left| \frac{\sigma_1}{\sigma_2} \right|^n \quad (11)$$

And then:

$$n = \frac{\ln\left(\frac{\dot{\theta}_1}{\dot{\theta}_2}\right)}{\ln\left(\frac{\sigma_1}{\sigma_2}\right)} \quad (12).$$

If quick pressure step profile is imposed during the sintering (see Figure 1), the stress exponent value of n can be determined by the measurement the $\dot{\theta}_i$ for different σ_i before and after the pressure “jump” [30]. This method is used to determine the stress exponent “ n ”.

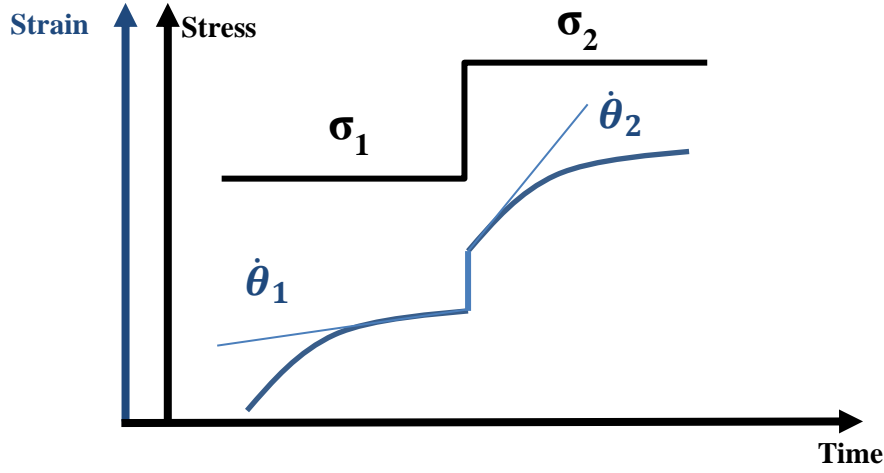


Figure 1: Description of the stress exponent identification by spark plasma sintering using the “stepwise” pressure approach.

2.3. Identification of Q and A_0 and calibration of ψ and φ by linear regression.

From the analytic expression of spark plasma sintering (10) isolating the temperature dependent terms and taking the logarithm give the following linear regression equation [29,32].

$$Y = \ln \left(\frac{T|\dot{\theta}|}{(\psi + \frac{2}{3}\varphi)^{\frac{-n-1}{2}} (1-\theta)^{\frac{3-n}{2}} |\sigma_z|^n} \right) = \ln(A_0) - \frac{Q}{RT} \quad (16)$$

Using hypotheses on the shear and bulk moduli in the left-hand side of the equation (16), this regression allows to determine the sintering activation energy (Q) by the slope of the curve and the term (A_0) by the exponent of the curve’s origin. In a first stage, above regression equation left-hand side uses the theoretical Skorohod’s moduli [31] below.

$$\psi = \left(\frac{2}{3}\right) \frac{(1-\theta)^3}{\theta} \quad (17)$$

$$\varphi = (1 - \theta)^2 \quad (18)$$

Plotting, for each heating rate, Y term vs $1/RT$, the slope of the linear regression gives Q value and the origin should converge to a same value of $\ln(A_0)$ that should be unique. Because

Skorohod's moduli are theoretical approximations, the regression of the different heating rates (that should be unique) may be dispersed. At this stage, the moduli can be modified using the following Skorohod's modified moduli expression [33,34].

$$\varphi = \left(1 - \frac{\theta}{\theta_{ci}}\right)^2 \quad (19)$$

$$\psi = \left(\frac{2}{3}\right) \frac{(\theta_{ci}-\theta)^\gamma}{(\theta-\theta_{cf})^\zeta} \quad (20)$$

With θ_{ci} the initial critical porosity generally close and slightly higher than the initial porosity, θ_{cf} the final stage critical porosity, which represents the level of macro-porosity that eventually remains after sintering and which cannot be eliminated and γ, ζ are additional adjustable exponents (≥ 1). Latter adjustable parameters can be modified from Skorohod's base up to obtain all regression curves together as one curve.

3. Experiment and method

All experiments have been realized with the SPS apparatus “FCT HPD25” with graphite grade Mersen 2333 dies, punches and spacers. All samples are made of Ti-6Al-4V powder grade 5 supplied from AP&C. Powder particle size has been measured by an optical granulometer Mastersizer 2000. As shown in Figure 2.a., the particle size distribution is in the range of 10 to 100 μm with a median size of 34 μm . The SEM image, Figure 2.b., shows powder that particles are mostly spherical.

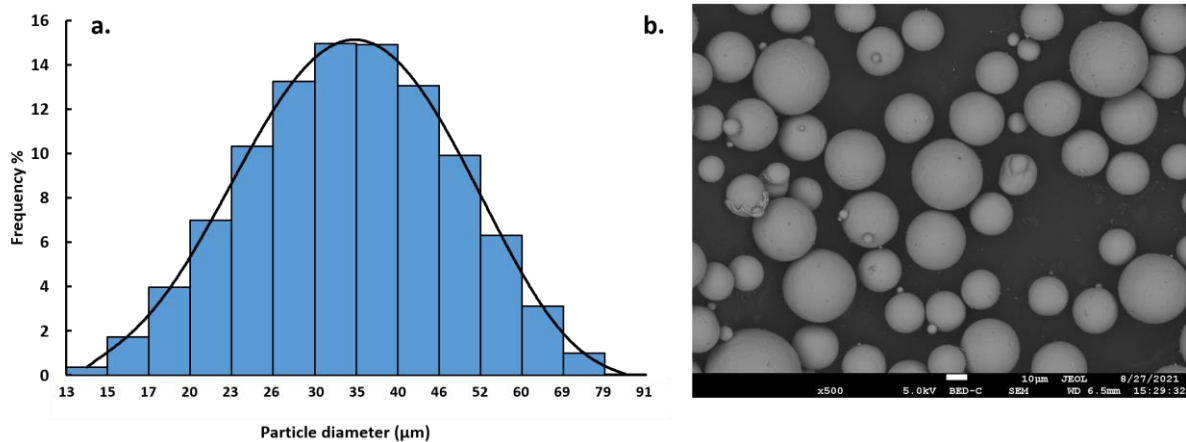


Figure 2: a. Ti-6Al-4V powder particle size distribution measured by optical granulometer. b. SEM image showing the morphology of the Ti-6Al-4V powder particles.

For all experiments, temperatures have been measured with a K type thermocouple located inside the graphite die at 3 mm of the inner die surface.

For the stress exponent (n) determination, 3 isothermal tests were performed at 885 K, 1033 K and 1153 K. During these tests, samples of 10 g were subjected to two rapid pressure increases from 5 kN to 10 kN and then from 10 kN to 15 kN. These “jump” pressures were as fast as the SPS machine would allow, ~ 1 s. The inner diameter of the dies for those tests was 20 mm. measuring the porosity elimination rate before and after the “jump” pressures allows to determine the stress exponent value by equation (12).

For the sintering study, three samples of 5 g were heated from ambient temperature (near 20 $^{\circ}\text{C}$) up to 1080 $^{\circ}\text{C}$ with different heating rates: 50 K/min, 100 K/min and 200 K /min and under a

constant pressure of 50 MPa in a 15 mm inner diameter die. Pressure has been settled at ambient temperature before the heating. In order to consider a temperature as close as possible to the real temperature experienced by the samples, the temperature measured by the thermocouple was corrected by means of a finite element simulation (FEM) [35,36]. The details of this simulation are fully detailed in a previous paper [37]. After identification of the “ n ”, the regression study using equation (16) is conducted to determine Q , A_0 while adjusting the shear and bulk moduli value to obtain three unique regression curves.

A boron nitride layer sprayed on the graphite paper located between the punchers and the sample electrically insulates the samples for all experiments. This insulation prevents electrical current from flowing through the Ti-6Al-4V sample and thus avoids potential electrical effects that may disturb the sintering kinetics [38,39].

After identification of all the sintering parameters n , Q , A_0 , φ , ψ , the 3 sintering tests were simulated to compare the simulated curves with the experimental data. All sintering analytic modeling have been realized on GNU Octave 5.1.0. Afterward, the 3D sintering simulations were made using COMSOL multiphysics 5.0.

In order to produce truncated conical shapes by SPS [4], conical skeleton submold with a wall thickness of 0.75 mm were printed using a profession ceramics stereolithography printer, the carmaker 100 from 3DCERAM SINTO®. An alumina resin “3DMix AL-E02” was used to ease the shape ejection after SPS. The Ti-6Al-4V sintered cone parts were scanned with an EinScan-SP 3D scanner with the accuracy of 30 μm .

To reveal their microstructure, samples were polished and etched with a solution of chloric acid, fluoric acid and nitric acid: 30% HCl; 10% HF; 10% HNO₃; 50% H₂O. Vickers hardness was measured with a “MICROPRESI MATSUTAWA MMTx7” under a 0.5 kgF load.

4. Results and discussions

4.1. Ti-6Al-4V samples presentation

As described in section 3, three SPS tests were performed at different heating rates: 50 °C/min, 100 °C/min and 200 °C/min. The sintering curves of Ti-6Al-4V samples for the different heating rates are presented in Figure 3. To evaluate the sample temperature with the best possible accuracy, simulations have been performed to correct these apparent temperatures. The details of this simulation are available in a previous published paper [37].

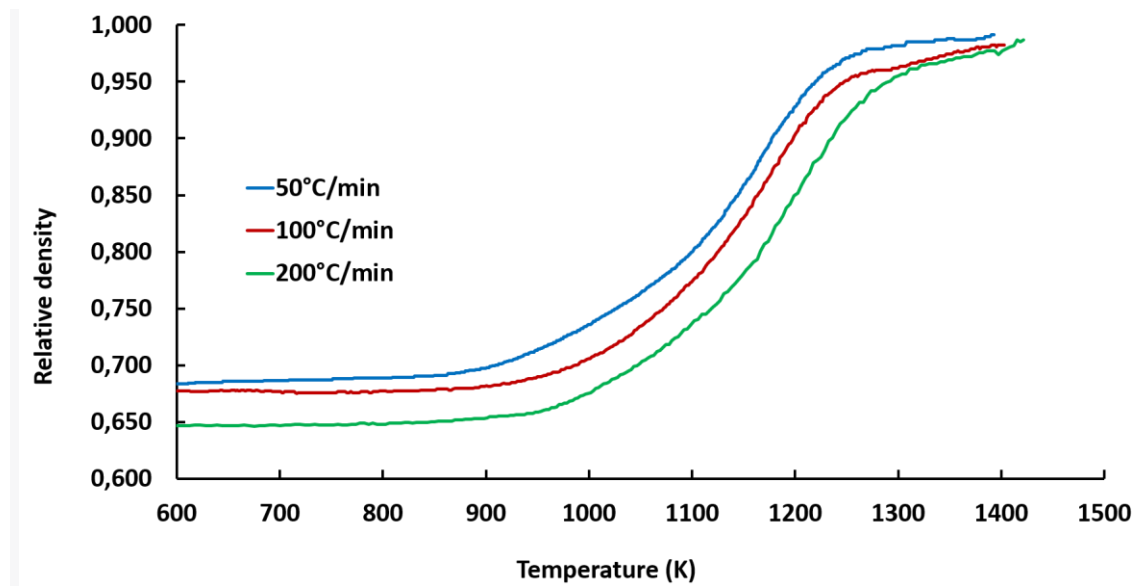


Figure 3: SPS sintering curves of the Ti-6Al-4V samples for three different heating rates with temperatures corrected from simulations.

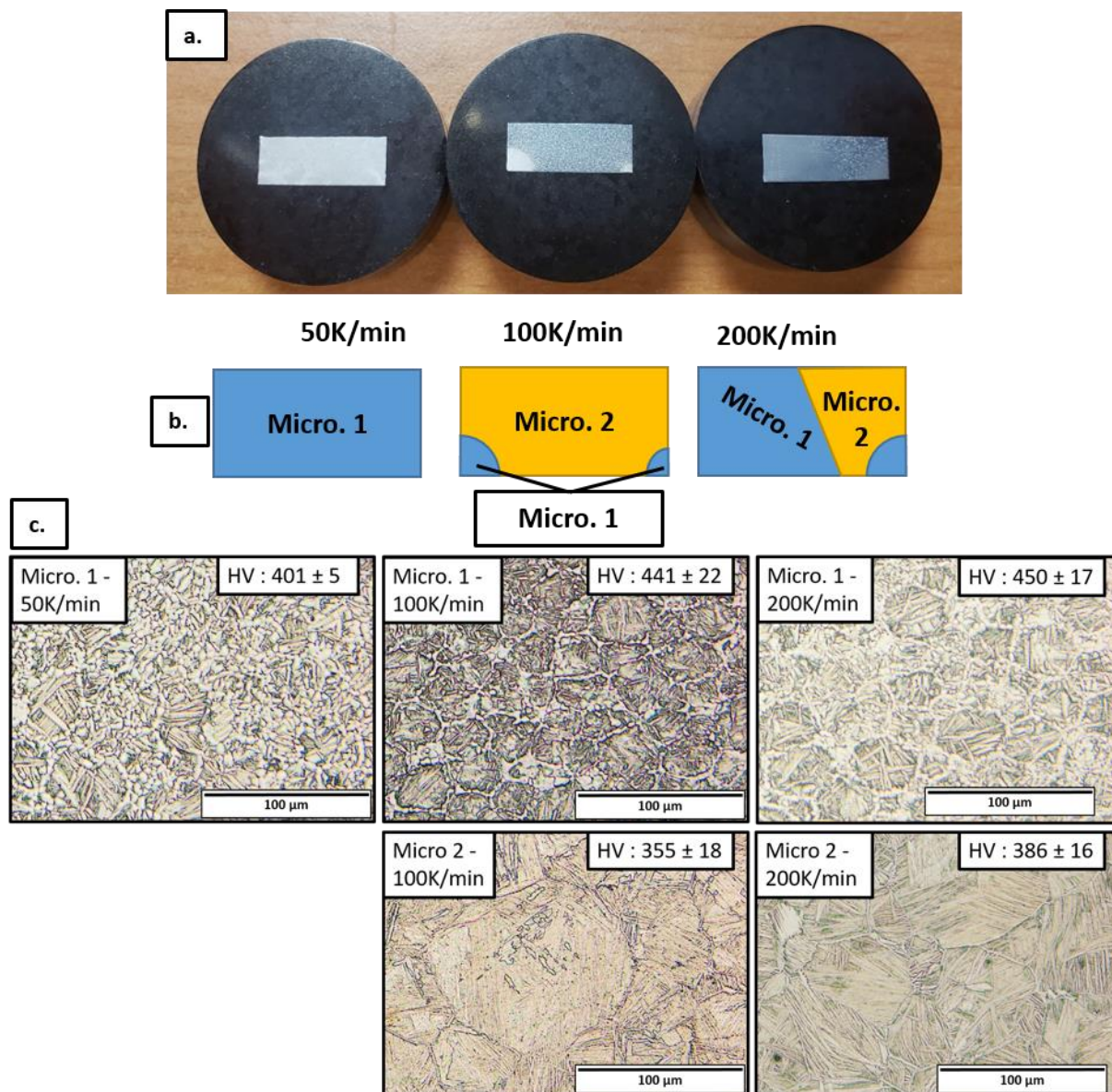


Figure 4: a. Photography of the samples; the difference of microstructure is visible. b. Schematic representation of the microstructures, the abbreviation “Micro.” stands for “microstructure”. c. Metallography of the sample: the two microstructures correspond to an acicular $\alpha+\beta$ microstructure.

As shown on Figure 4.a, two different zones are observed: “micro 1” in lighter color and another one, “micro 2”, darker. Depending on the experimental conditions, those two zones are differently localized within the material, as shown schematically in Figure 4.b. The microstructures were revealed by etching for phase identification as shown Figure 4.c. Otherwise, Vickers hardness (values are indicated in top right of each optical images in figure 4) was measured to correlate microstructures to mechanical properties. Despite the fact that the appearance of the two locations looks different, both are made from an α phase embedded in

the β matrix [40–42]. It is quite sure that all samples have exceeded the β transus temperature since the maximum temperature undergone by the samples is 1400K and the maximum control temperature measured in the die is 1295K, well above the β transus 1195K. On the micro 1, the colonies of α platelets and the α phase decorating the β/β grain boundaries are coarser than on the micro 2. This indicates a difference in cooling rate between zones in the same sample. It seems that the zone of the samples with the micro 1 has cooled down faster than the zone with micro 2. As Ti-6Al-4V alloy has a low thermal conductivity, these cooling rate heterogeneities are expected [43]. Even if those microstructures are not well controlled, the only purpose of this work was to determine the sintering parameters of Ti-6Al-4V alloy. In addition, the hardness measurements are consistent with those reported in the scientific community for such a microstructure (300-400HV) [44–46]. However, the micro 1 seems to have a high hardness for Ti-6Al-4V, possibly due to rapid cooling involving lower grain sizes. When increasing the heating rate the hardness of micro 1 slightly increases. The most probable explanation is faster cooling rates resulting from the lower spacer temperatures for high heating rates.

4.2. Sintering parameter determination

For some materials like Ti-6Al-4V alloy, the mechanism governing the pressure assisted sintering evolves with temperature [47,48]. The stress exponent " n " is an indicator of these mechanisms and has an important impact on the sintering behavior of the materials. Therefore, the evolution of the stress exponent " n " of Ti-6Al-4V as a function of temperature was first studied.

As presented in section 2.3, the value of n has been determined by measuring the $\dot{\theta}_i$ for different values of σ_i at same θ and for different temperatures. For each isothermal test, two "jumps" in pressure allowed to extract two values of the exponent " n " for each considered temperature [30]. The " n " values and the SPS tests are presented on Table 1 and in Figure 5.a, respectively. These values give an indication of the evolution of stress exponent " n " as a function of temperature during sintering. However, these 6 values are not sufficient. It is necessary to

integrate a continuous evolution of stress exponent "n" as a function of temperature. Since a value of stress exponent "n" too high or lower than 1 does not make physical sense, a sigmoid function has been chosen to fit the "n" temperature evolution, see in Figure 5.b. The fit equation is reported below:

$$n = \left(1 - \frac{1}{1 + e^{-0.007 \times (T^\circ(K) - 910)}}\right) \times 4.985 \quad (21)$$

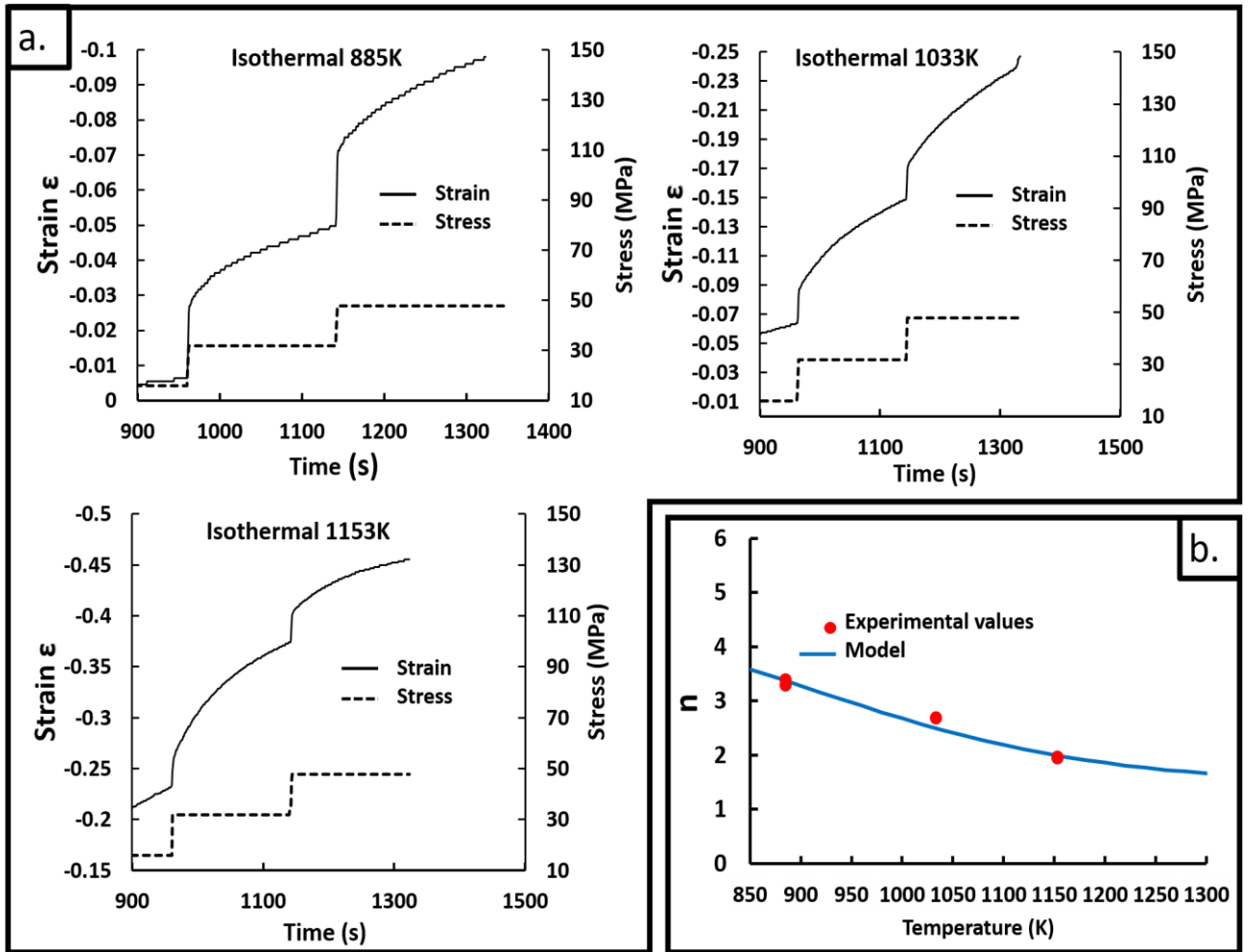


Figure 5: Stress exponent "n" determination by a. multiple pressure step SPS at different temperatures: 885K, 1033K and 1153K. b. obtained Ti-6Al-4V stress exponent "n" model evolution as a function of temperature.

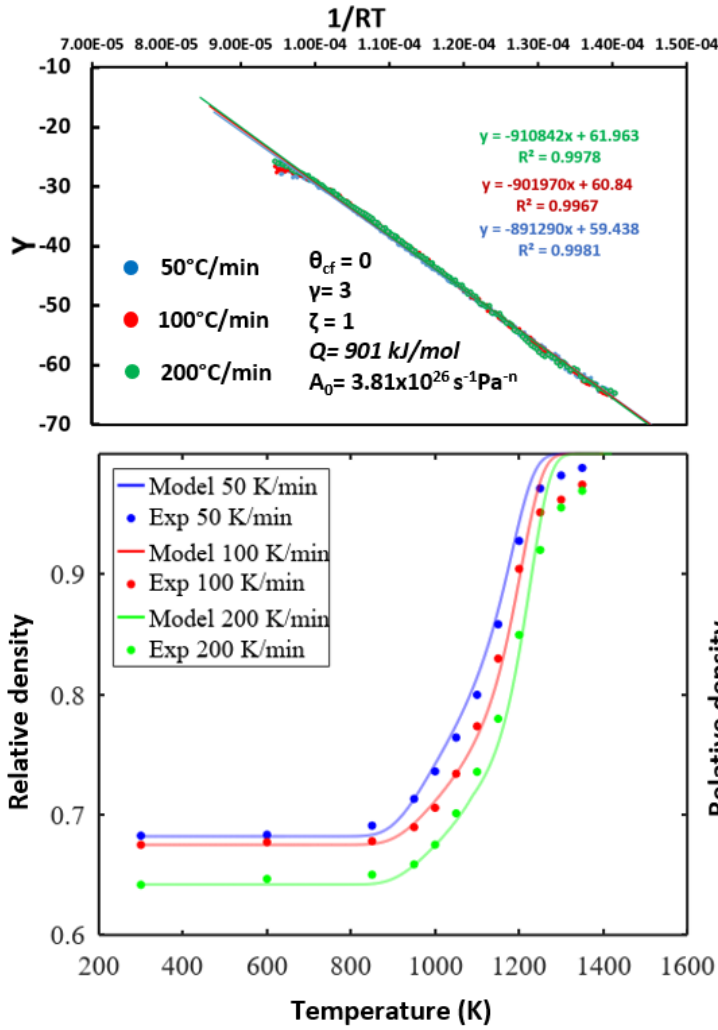
Temperature (K)	885	1033	1153
n value 1	3.28	2.70	1.97
n value 2	3.39	2.68	1.95

Table 1: Stress exponent "n" values of the Ti-6Al-4V alloy at different temperatures.

With the evolution of the stress exponent as a function of temperature integrated in regression equation (16), the activation energy “Q” and A_0 parameter have been determined by linear regression of each heating rate in the Y vs $1/RT$ graph reported in Figure 6. The first model reported in Figure 6a has been determined considering the starting point is the theoretical Skorohod’s moduli [31] (17,18).

“Q” and A_0 values was found to be 901 kJ.mol^{-1} and $3.81.10^{26} \text{ s}^{-1}\text{Pa}^{-n}$, respectively. This activation energy value is significantly higher than the activation energy value of material whose sintering is governed by only one sintering mechanism ($n=2$ constant $\rightarrow 416 \text{ kJ.mol}^{-1}$) [27]. However, in the case of Ti-6Al-4V alloy where the n evolves during the sintering, this activation energy reflects the disturbance of “ n ” evolution with temperature. This sintering model gives acceptable fits of the experimental data when analytic modeling is done (see lower part of Figure 6). However, to optimize as far as possible the model in final stage sintering where more discrepancies are present, the modified Skorohod’s moduli expression (19,20) was considered with specific θ_f (final porosity), ζ and γ parameters for Ti-6Al-4V, see Figure 6b. The set of adjusted parameters allows to better fit the final stage without modifying too much the apparent activation energy are $\theta_f=0.005$, $\zeta=2$ and $\gamma=1$. With these considerations, the values of “Q” and A_0 are 912 kJ.mol^{-1} and $3.65.10^{28} \text{ s}^{-1}\text{Pa}^{-n}$, respectively.

a. Theoretical Skorohod's moduli



b. Modified Skorohod's moduli

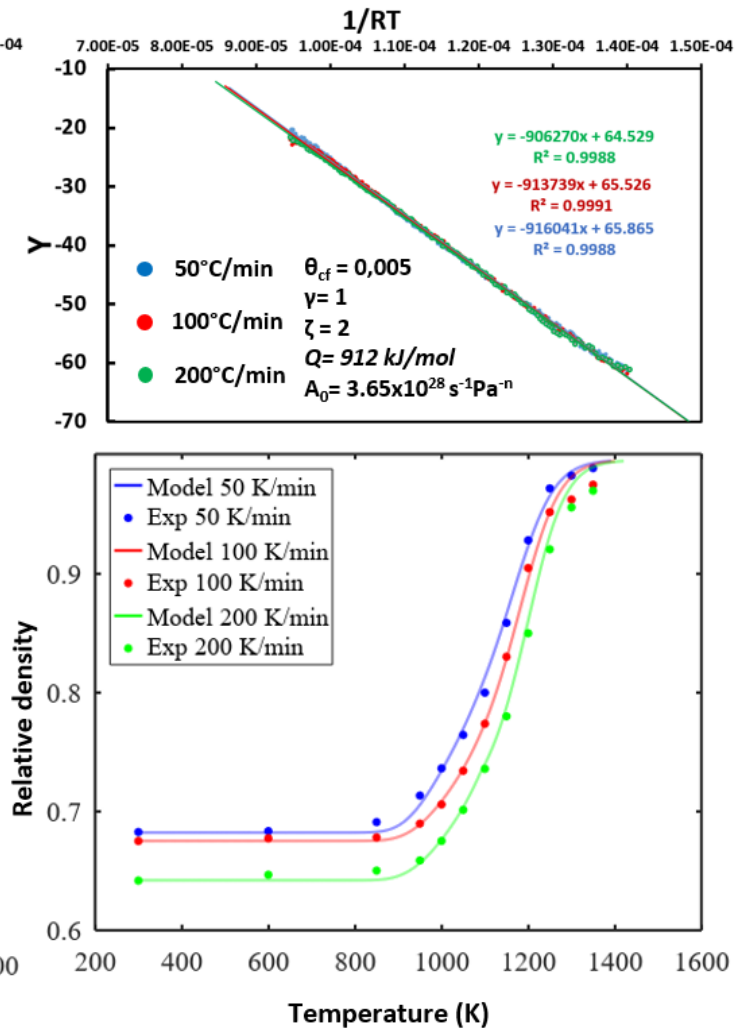


Figure 6: SPS sintering model of Ti-6Al-4V linear regression, simulation and experimental data of Ti-6Al-4V SPS sintering with (a.) theoretical Skorohod's moduli and (b.) modified Skorohod moduli.

5. Application of the sintering model on complex shape sintering case

5.1. Complex shape sintering setup

The interface method to produce complex shapes by SPS involves creating an assembly of two powder zones separated by a deformable interface [4]. The whole assembly is generally a cylinder that can be very easily and uniformly sintered by SPS (see the scheme in Figure 7.a). One of these two powders is called the “working” powder and will form the final complex-shaped part after densification, while the other powder is called the sacrificial powder, and serves no other purpose than homogenizing the shrinkage on the different parts of the assembly

under uniaxial compression. The interface between the working and sacrificial powders helps the post-sintering ejection of the complex shape citing inside the assembly. The latter is printed by stereolithography from an alumina charged resin (see the green shape in Figure 7.b). The organic part of the ceramic resin is partially degraded during the beginning of the SPS heating into graphite which transform the printed submold complex interfaces into a graphite/alumina interface. The fact that the working and sacrificial powders sinter with identical densification behavior causes the powder assembly to behave like a homogeneous medium. The final complex shape can be predicted by a simple elongation factor in the pressure direction that depends on the initial and final relative densities ($D_{\text{final}}/D_{\text{initial}}$). The only source of shape errors is the discrepancy caused by the thin interface, thermal gradients and the eventual friction between the parts. In previous work, it has been shown that SPS powder/graphite foil/die multiple interfaces have very limited friction effects and thus low impact on the densification of materials [49]. The finite element simulation of the multiple powder assembly can be used to study the impact of the interface on the shape deformations [15,17].

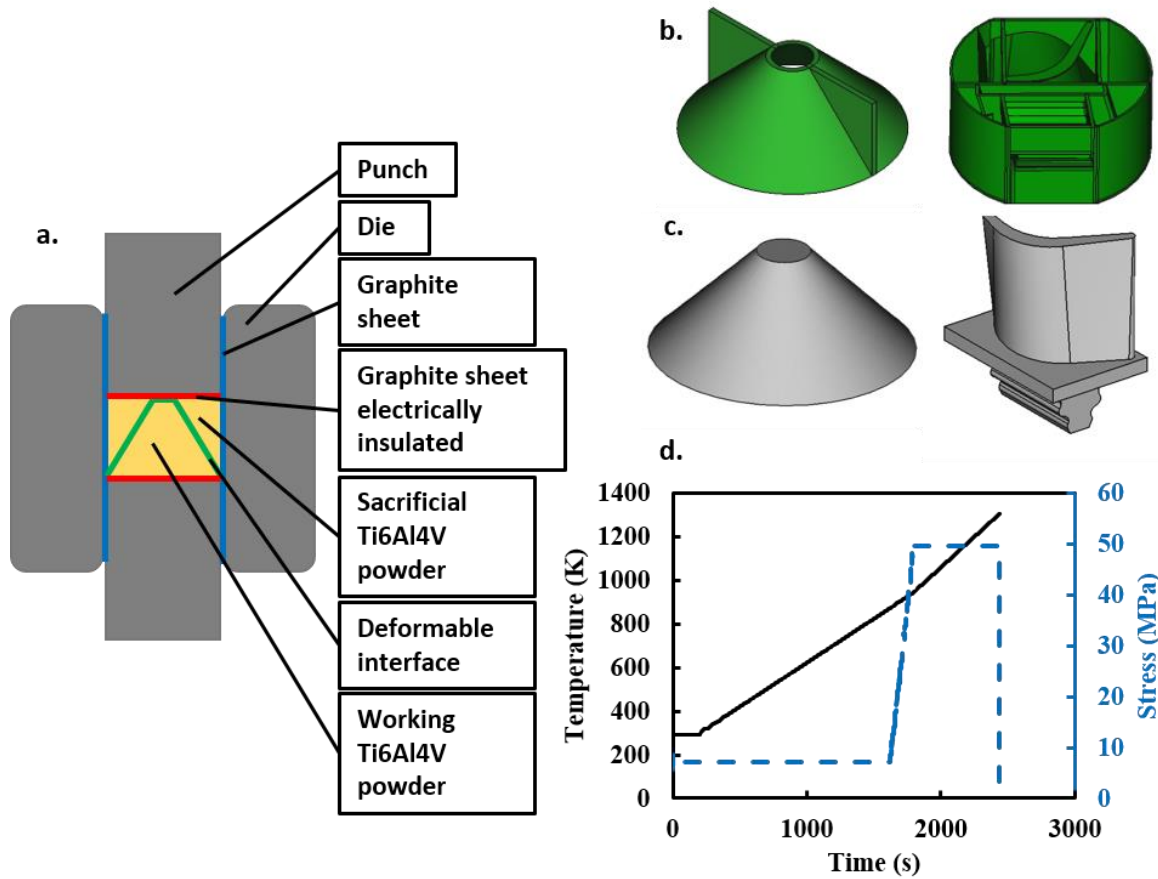


Figure 7: a. Scheme of the interface method for the fabrication of complex shapes in SPS, case of the cone shape b. 3D printed deformable interface used in this study for the cone and the thin turbine blade shapes, c. corresponding 3D targeted shapes, d. thermal and mechanical cycle undergone by the sample.

In this application, the two produced complex shapes are a simple cone and a turbine blade. The 3D virtual objects of the blade and the cone are reported in the Figure 7.c. The thin walls on the sides of the cone interfaces are necessary for its proper 3D printing by stereolithography. For the turbine blade, several walls have been added in the sacrificial zones to ease the post-SPS turbine blade ejection. The sample temperature was raised to 875K at 25K/min under a uniaxial stress of 7 MPa (interface partial debinding), and then up to 1300K at 50K/min under a stress of 50 MPa (sintering). The sample was then cooled using the cooling circuits of the SPS under a stress of 7 MPa in a mode that does not allow for temperature measurement during cooling (see Figure 7 .d).

5.2. Cone shape case

Figure 8a is a 3D scan of the cone after sintering and ejection, revealing several shape defects. Under the 3D printed side wall zone, there is a depression in the cone surface. This suggests that the wall interface is slightly more resistant to sintering than the powder. Moreover, the cone sides are slightly curved instead of being straight. The cone was cut and etched to reveal its microstructure, as presented in Figure 8b. The microstructure of the cone consists of a coarse, fully lamellar $\alpha+\beta$ colonies, except at its edges. A skin effect seems to arise near the surface of the cone that is in contact with the interface during sintering. A 20 μm layer appears with a coarser α phase that tends towards an equiaxed morphology. This phenomenon is likely due to a surface contamination in carbon (α -stabilizer element) causing an increase in the β transus temperature and hence the appearance of this α -case layer.

Vickers hardness was measured from the edge towards the core of the sample to reveal any potential gradients in mechanical properties (see Figure 8.c). Unfortunately, the 20 μm surface layer was too thin and too close of the cone edge to measure its hardness. Hardness does not appear to vary with distance from the edge of the sample. The cone exhibits a stable hardness of $\text{HV}_{0.5} = 379 \pm 14$ in average, which is consistent with its microstructure [44–46].

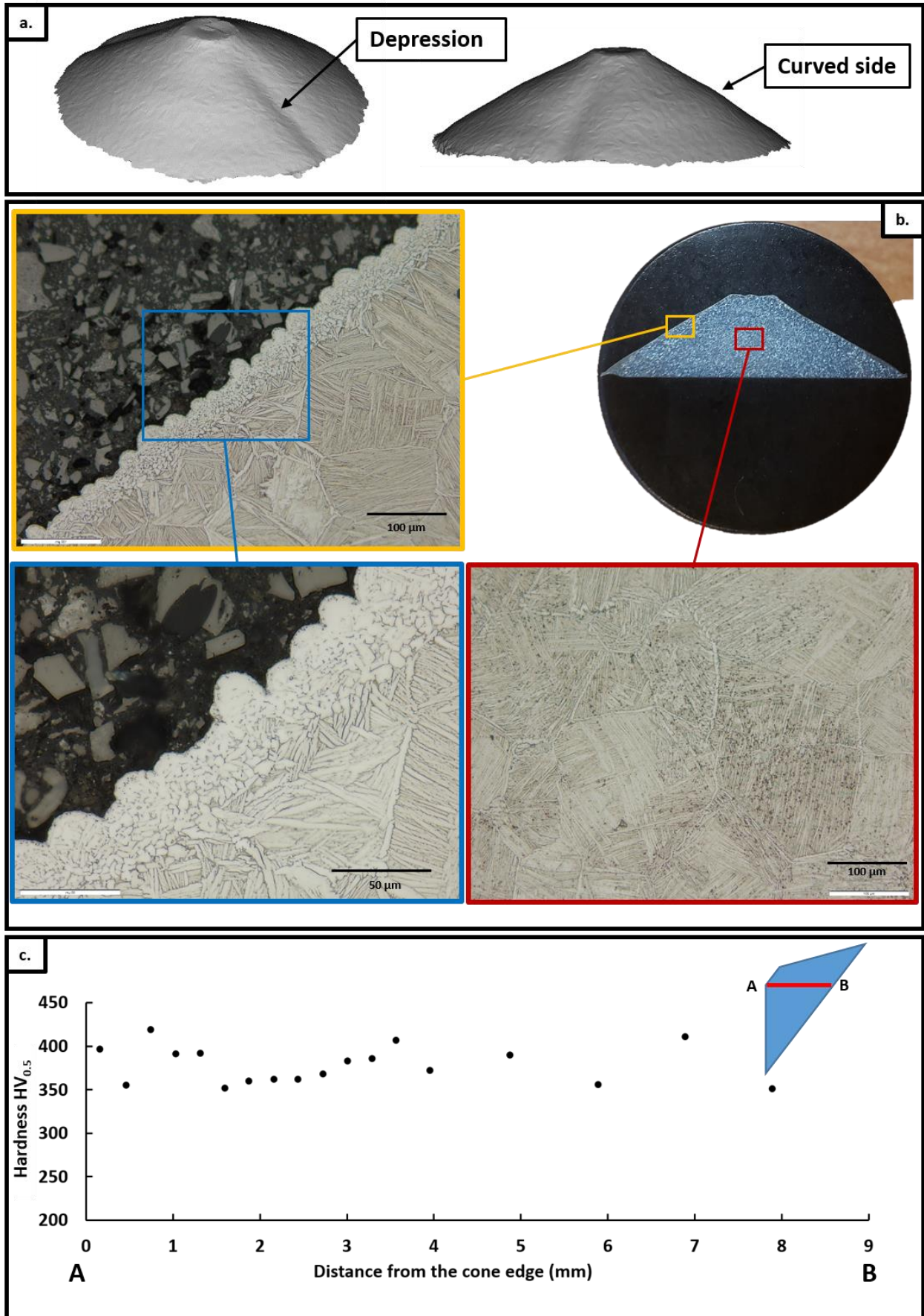


Figure 8: a. 3D Scan of the cone after sintering and ejection. b. Cut cone with a fully lamellar $\alpha+\beta$ microstructure in the core and a skin effect of equiaxed α grains on the edge. c. Vickers hardness measured from the edge to the core of the sample under 0.5 KgF.

In order to investigate the possible presence of pollution or chemical composition gradients, SEM-EDS analyses were performed. Figure 9.a shows a SEM image of the cone where the skin effect is visible. An EDS analysis was carried out along the red arrow. The qualitative line profiles of solute elements from the skin to the core are presented in Figure 9.b. A qualitative comparison can be made between the skin and the core. The comparison suggests the skin area is richer in carbon than the core. The content of the other solute elements does not significantly change. This analysis seems to confirm the hypothesis of a α -case layer due to a carbon surface contamination.

Figure 9.c is another SEM micrograph of the cone edge. The microstructural differences between the skin and the core are still visible but the image reveals another thinnest skin of a few microns on the extreme edge of the cone. Another EDS analysis (EDS map) was realized in a similar area to highlight the partitioning of solute elements as presented in Figure 9.d. This analysis reveals that the thin skin (in contact with the interface) is richer in aluminum than the core of the cone. It also suggests the presence of titanium carbide that precipitates at the grain boundaries.

As the alumina resin interface degrades into a graphite/alumina interface during the process, this interface may be the source of carbon explaining the precipitation of titanium carbide that seems to appear at the grain boundaries of the skin zone. The contact with alumina seems to be the main origin of the micron-sized aluminum-rich phase. These findings indicate a chemical contamination from the interface towards the sample over a short distance from the surface. However, this interface contamination is very limited and restrained to a 20 μm skin. The addition of a small carbon content is known to lead to the precipitation of carbides [ref]. In addition to precipitation hardening, these carbides reduce oxygen segregation at grain boundaries, forming Ti(CO). This reduction in oxygen content prevents or limits the formation of α phase at grain boundaries, leading to a significant increase in the alloy's ductility [ref].

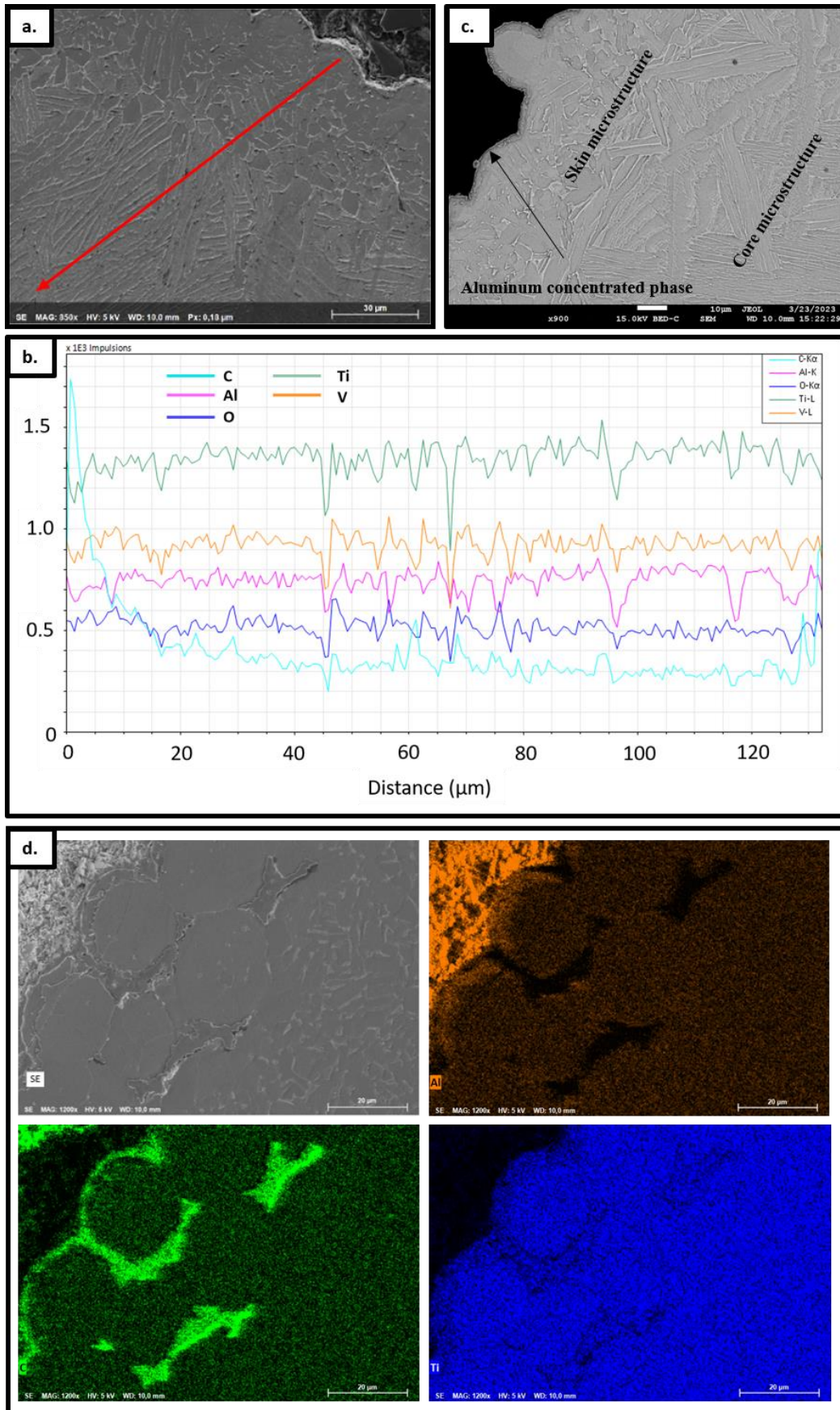


Figure 9: SEM-EDS analyses of Ti-6Al-4V cone sintered with SPS: a. Area of composition analysis along the red arrow. b. Composition analysis: the carbon concentration is higher on the 20 μm under the cone surface. c. Image of the cone surface: presence of a second phase under the cone surface. d. Chemical analysis of another similar sample: the second phase is enriched in aluminum and titanium carbides at grain boundaries.

5.3. Turbine blade case analysis

Figure 10.a shows the pictures of the sintered turbine blade revealing several shape defects. A part of the twist near the vertical walls is flattened, and on its basis, the twist seems to undergo shrinkage. Therefore, the plate is slightly bent. On the surface of the blade, curved lines forming a slight roughness are visible. These lines correspond to the surface finish of the 3D printed interface. Each line is a cured layer (50 μm) during stereolithography. This roughness is transmitted from the interface to the blade during sintering. On the profile of the cut turbine blade (in Figure 10.b), the shape of the twist is more visible. Indeed, the twist undergoes shrinkage on its basis and on its top.

In the Figure 10.c, the microstructure of the cut blade is revealed by etching. All the blade shows an acicular $\alpha+\beta$ microstructure like for the cone sample previously presented . The skin effect detected earlier is also noticeable on the edges of the blade. Since the interface of the cone and the blade are printed with the same resin, the blade is also subjected to surface pollution resulting from the contact with the interface.

The Vickers hardness has been measured on the blade section. Figure 10.d shows the hardness measurement at different locations on the blade section. The blade shows a homogeneous hardness of $\text{HV}_{0.5} = 387 \pm 14$, which is consistent with the cone hardness and its microstructure [44–46].

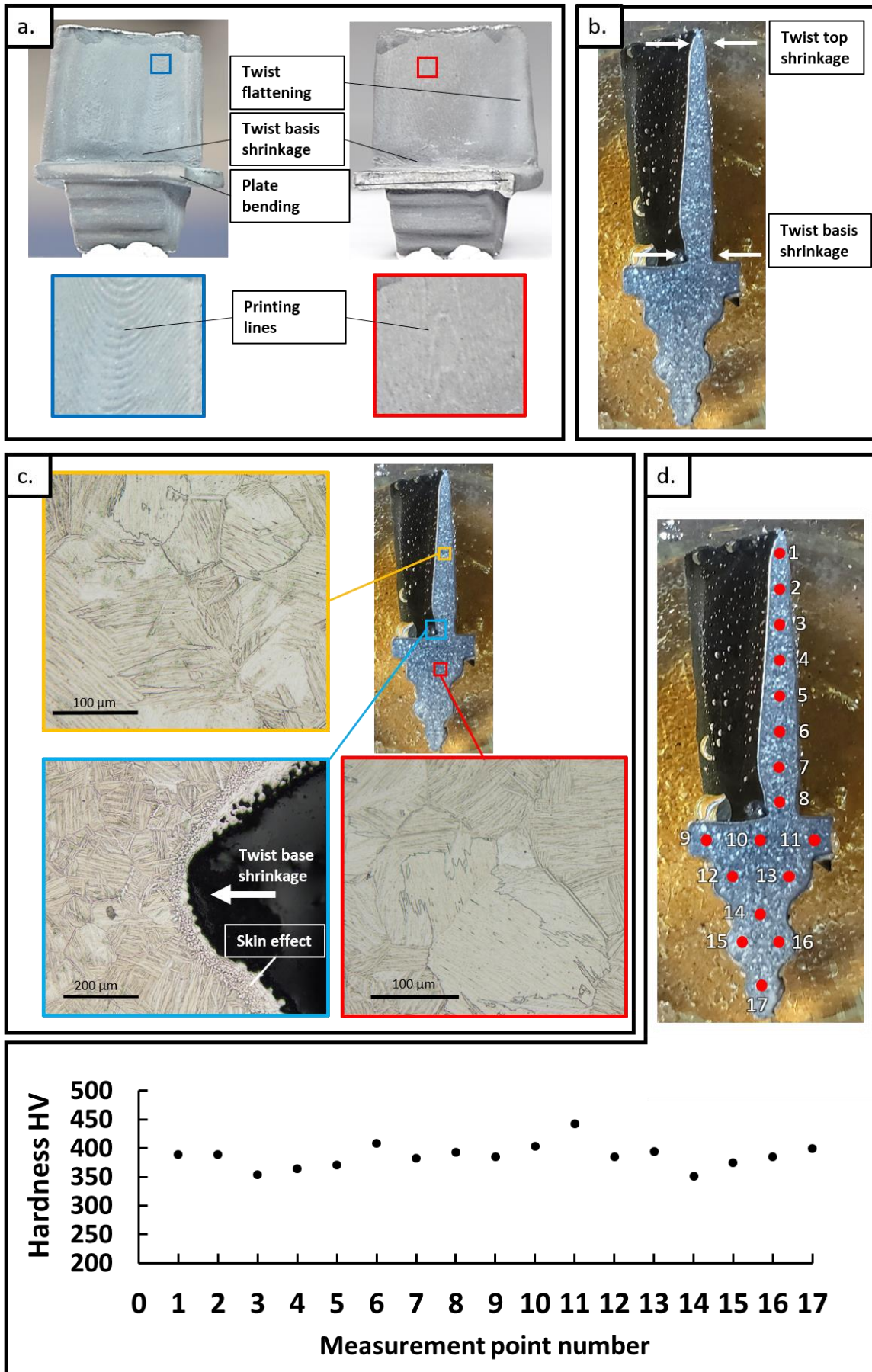


Figure 10 : a. Pictures of the sintered turbine blade. b. Picture of the cut turbine blade. c. Microstructure at different locations of the cut turbine blade. d. Vickers hardness measurement on the blade section.

5.4. Cone sintering simulation using previously presented model

The SPS densification of the powder in an assembly to produce a conical part has been simulated to estimate virtually the deformations of the interface on the cone shape observed on the real part (see Figure 11a). Due to the shape symmetry, the simulation was made on a quarter of the assembly to reduce the computation time (see Figure 11.b). The simulated relative density evolution during the cycle is reported in Figure 11.c. It shows the compaction of the titanium alloy powder and of the 3D printed interface. The 3D printed interface was modeled using an initial relative density of 0.75. To simulate an interface with a higher sintering resistance than the powder with a high computational stability, the same property of the powder was selected and a higher activation energy was selected up to obtain the same magnitude in the distortions that is observed experimentally. The calibrated activation energy is $940 \text{ kJ}\cdot\text{mol}^{-1}$. In the case of the cone, the same distortions of the interface can be clearly seen at the final stage. The simulated cone shows the depression under the interface walls and the slightly curved shape of its sides, see Figure 11.a. and c.

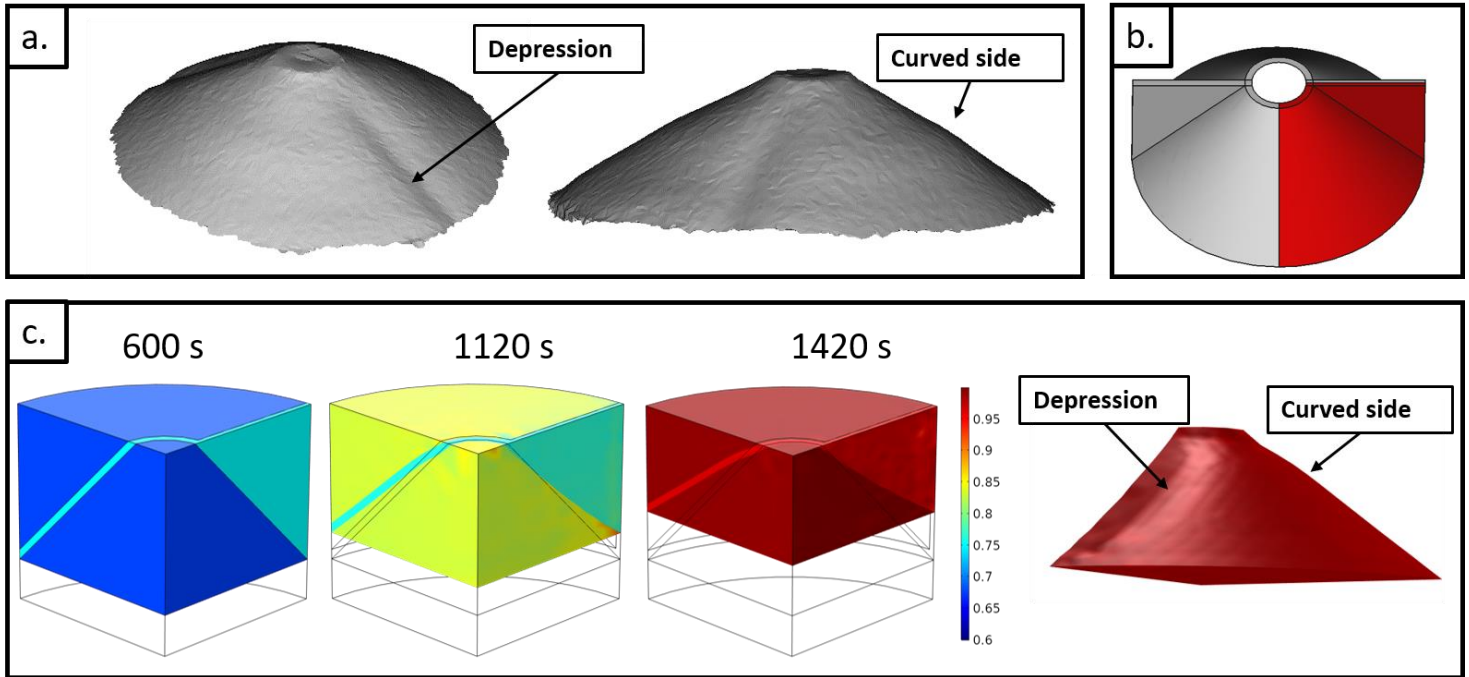


Figure 11: a. 3D Scan of the SPS cone shape b. scheme of a portion of the part that was simulated (in red) due to the symmetry of the shape c. Result of the sintering simulation of the quarter of the conical powder assembly, with on the right, the cone quarter final shape in red.

5.5. Blade sintering simulation using previously presented model

The same SPS densification simulation has been done for the turbine blade powder assembly. Figure 12.a shows the simulated densification over time. In Figure 12.b, the comparison between the experimentally produced and the simulated blade shows that the simulation manages to predict the twist flattening and the plate bending. The experimental blade section and simulated powder assembly section are reported in the Figure 12.c. The distortions of the interface noticeable in the simulated powder assembly section explain the shrinkage of the twist top and basis. These comparisons between experimentally produced and simulated turbine blades illustrate that the simulation model developed allows identifying shape defects for complex shape sintering.

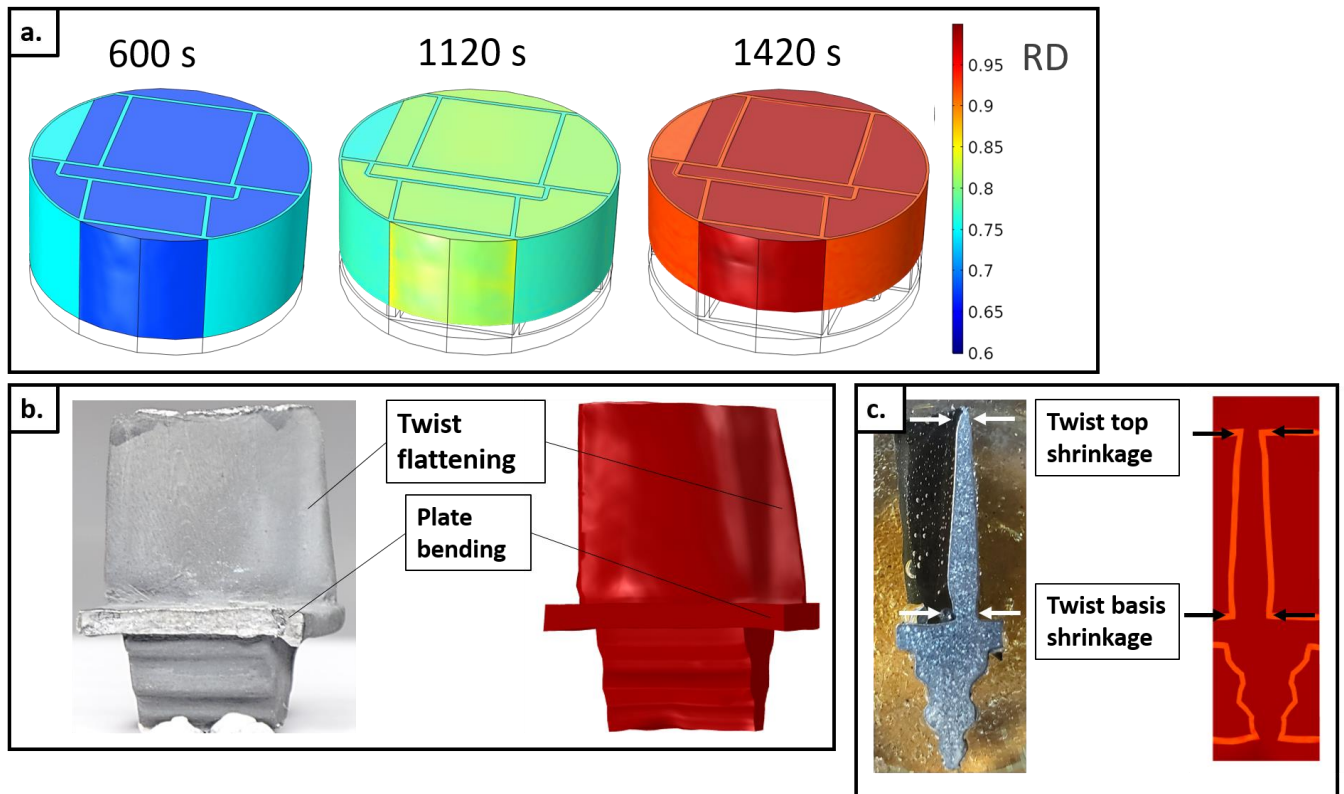


Figure 12: a. Result of the sintering simulation of the whole blade powder assembly. b. Picture of the experimentally produced blade and the simulated blade for comparison of shape defects. c. Picture of the experimentally blade section and simulated blade section for shape defects comparison.

6. Conclusion

In this study, the SPS sintering behavior of a Ti-6Al-4V complex shapes was studied by several analyses and experiments. All the material parameters necessary to build a sintering model based on Skorohod-Olevsky model of Ti-6Al-4V have been determined using the analysis method using model regression and SPS experiments at different heating rates and different pressures. The stress sensitivity analysis reveals a sintering mechanistic evolution with temperature from dislocation based mechanisms at low temperature toward diffusional mechanisms at high temperature. This transition has a strong impact on the sintering behavior and imply higher value of apparent activation energy. To perfectly reproduce the sintering curves, the Skorohod's theoretical shear and bulk moduli exponents have been adjusted. Once the sintering model was established, it was used to simulate the defects present during SPS of complex shapes. Comparison between the experimental and simulation reveals that the latter

succeeds in reproducing the distortions observed on the cone and turbine blade shaped parts produced by SPS. The analysis of the cone has shown a fully dense and homogeneous fully lamellar microstructure and a 20 μm α -case layer near the interface with second aluminum-rich second skin of few μm in contact with the interface. The sintered blade exhibited the same microstructure and the same skin effects probably due to a surface contamination from the degraded interface. This study demonstrates the feasibility of highly complex shapes production by SPS. Coupling the stereolithography 3D printed ceramics charged interface with SPS post-treatment greatly facilitates this interface method for rapid prototyping of metal objects.

7. Acknowledgements

The authors thank the Normandy RIN Region Project DEFORMINT n°2019111818193100000210000257 for the financial support of this Study and Christelle Bilot for the SEM images.

References

- [1] T. Voisin, J.P. Monchoux, L. Durand, N. Karnatak, M. Thomas, A. Couret, An Innovative Way to Produce γ -TiAl Blades: Spark Plasma Sintering, *Adv. Eng. Mater.* 17 (2015) 1408–1413. <https://doi.org/10.1002/adem.201500019>.
- [2] K. Srinagesh, Powder metallurgy of iron and steel, *Choice Rev. Online.* 36 (1998) 36-0981-36–0981. <https://doi.org/10.5860/CHOICE.36-0981>.
- [3] C. Manière, L. Durand, A. Weibel, G. Chevallier, C. Estournès, A sacrificial material approach for spark plasma sintering of complex shapes, *Scr. Mater.* 124 (2016) 126–128. <https://doi.org/10.1016/j.scriptamat.2016.07.006>.
- [4] C. Manière, E. Nigito, L. Durand, A. Weibel, Y. Beynet, C. Estournès, Spark plasma sintering and complex shapes: The deformed interfaces approach, *Powder Technol.* 320 (2017) 340–345. <https://doi.org/10.1016/j.powtec.2017.07.048>.
- [5] C. Manière, E.A. Olevsky, In situ partially degradable separation interface for fabrication of complex near net shape objects by pressure assisted sintering, Patent US 2021/0016499 A1, US2021/0016499A1 WO2019/191299A1, 2018.
- [6] C. Manière, G. Lee, E.A. Olevsky, Flash sintering of complex shapes, *Appl. Mater. Today.* 26 (2022) 101293. <https://doi.org/10.1016/j.apmt.2021.101293>.
- [7] R.M. German, *Sintering Theory and Practice*, Wiley, Wiley, 1996.
- [8] J.J. Dunkley, Metal Powder Atomisation Methods for Modern Manufacturing, *Johnson Matthey Technol. Rev.* 63 (2019) 226–232. <https://doi.org/10.1595/205651319X15583434137356>.
- [9] R.M. German, *Powder Metallurgy Science*, Metal Powder Industries Federation, 1984.
- [10] T. Fedina, J. Sundqvist, J. Powell, A.F.H. Kaplan, A comparative study of water and gas atomized low alloy steel powders for additive manufacturing, *Addit. Manuf.* 36 (2020) 101675. <https://doi.org/10.1016/j.addma.2020.101675>.
- [11] S.H. Saheb, V.K. Durgam, A. Chandrashekhar, A review on metal powders in additive

- manufacturing, in: AIP Conf. Proc., 2020: p. 020018. <https://doi.org/10.1063/5.0026203>.
- [12] T. Hartwig, G. Veltl, F. Petzoldt, H. Kunze, R. Scholl, B. Kieback, Powders for metal injection molding, *J. Eur. Ceram. Soc.* 18 (1998) 1211–1216. [https://doi.org/10.1016/S0955-2219\(98\)00044-2](https://doi.org/10.1016/S0955-2219(98)00044-2).
- [13] N.L. Loh, K.Y. Sia, An overview of hot isostatic pressing, *J. Mater. Process. Technol.* 30 (1992) 45–65. [https://doi.org/10.1016/0924-0136\(92\)90038-T](https://doi.org/10.1016/0924-0136(92)90038-T).
- [14] Q. Bai, J. Lin, J. Jiang, T.A. Dean, J. Zou, G. Tian, A study of direct forging process for powder superalloys, *Mater. Sci. Eng. A.* 621 (2015) 68–75. <https://doi.org/10.1016/j.msea.2014.10.039>.
- [15] C. Manière, E. Torresani, E.A. Olevsky, Simultaneous spark plasma sintering of multiple complex shapes, *Materials (Basel)*. 12 (2019) 1–14. <https://doi.org/10.3390/ma12040557>.
- [16] M. Abouaf, J.L. Chenot, G. Raissou, P. Bauduin, Finite element simulation of hot isostatic pressing of metal powders, *Int. J. Numer. Methods Eng.* 25 (1988) 191–212. <https://doi.org/10.1002/nme.1620250116>.
- [17] A. Van der Laan, R. Epherre, G. Chevallier, Y. Beynet, A. Weibel, C. Estournès, Fully coupled electrothermal and mechanical simulation of the production of complex shapes by spark plasma sintering, *J. Eur. Ceram. Soc.* 41 (2021) 4252–4263. <https://doi.org/10.1016/j.jeurceramsoc.2021.02.010>.
- [18] C. Manière, L. Durand, A. Weibel, C. Estournès, Spark-plasma-sintering and finite element method: From the identification of the sintering parameters of a submicronic α -alumina powder to the development of complex shapes, *Acta Mater.* 102 (2016) 169–175. <https://doi.org/10.1016/j.actamat.2015.09.003>.
- [19] M.N.. Rahaman, *Sintering of Ceramics*, CRC Press, 2007.
- [20] N. Kurgan, Effects of sintering atmosphere on microstructure and mechanical property of sintered powder metallurgy 316L stainless steel, *Mater. Des.* 52 (2013) 995–998. <https://doi.org/10.1016/j.matdes.2013.06.035>.
- [21] E.A. Olevsky, Theory of sintering: From discrete to continuum, *Mater. Sci. Eng. R Reports.* 23 (1998) 41–100. [https://doi.org/10.1016/S0927-796X\(98\)00009-6](https://doi.org/10.1016/S0927-796X(98)00009-6).
- [22] M. Abouaf, J.L. Chenot, A numerical model for hot deformation of metal powders, *J. Theor. Appl. Mech.* 5 (1986) 121–140.
- [23] C. Manière, C. Harnois, S. Marinel, Porous stage assessment of pressure assisted sintering modeling parameters: a ceramic identification method insensitive to final stage grain growth disturbance, *Acta Mater.* 211 (2021) 116899. <https://doi.org/10.1016/j.actamat.2021.116899>.
- [24] C. Manière, E.A. Olevsky, Porosity dependence of powder compaction constitutive parameters: Determination based on spark plasma sintering tests, *Scr. Mater.* 141 (2017) 62–66. <https://doi.org/10.1016/j.scriptamat.2017.07.026>.
- [25] C. Nicolle, PhD, Mise en forme de poudre de bore par compression isostatique à chaud: détermination des propriétés rhéologiques et simulation numérique du procédé, Université de Bourgogne, France, 1999.
- [26] M. Abouaf, PhD, Modélisation de la compaction de poudres métalliques frittées, approches par la mécanique des milieux continus, Institut national polytechnique de Grenoble, 1985.
- [27] C. Manière, U. Kus, L. Durand, R. Mainguy, J. Huez, D. Delagnes, C. Estournès, Identification of the Norton-Green Compaction Model for the Prediction of the Ti–6Al–4V Densification During the Spark Plasma Sintering Process, *Adv. Eng. Mater.* 18 (2016) 1720–1727. <https://doi.org/10.1002/adem.201600348>.
- [28] D. Martins, F. Grumbach, C. Manière, P. Sallot, K. Mocellin, M. Bellet, C. Estournès, In-situ creep law determination for modeling Spark Plasma Sintering of TiAl 48-2-2 powder, *Intermetallics.* 86 (2017) 147–155. <https://doi.org/10.1016/j.intermet.2017.03.006>.
- [29] C. Manière, L. Durand, G. Chevallier, C. Estournès, A spark plasma sintering densification modeling approach: from polymer, metals to ceramics, *J. Mater. Sci.* 53 (2018) 7869–7876. <https://doi.org/10.1007/s10853-018-2096-8>.
- [30] W. Li, E.A. Olevsky, J. McKittrick, A.L. Maximenko, R.M. German, Densification mechanisms of spark plasma sintering: Multi-step pressure dilatometry, *J. Mater. Sci.* 47 (2012) 7036–7046. <https://doi.org/10.1007/s10853-012-6515-y>.
- [31] V.V. Skorohod, Rheological basis of the theory of sintering, *Nauk. Dumka, Kiev.* (1972).
- [32] J.S. Diatta, C. Couder, C. Harnois, S. Marinel, C. Manière, Modeling spark plasma sintering of zirconia with prediction of final stage high densification rate, *Mater. Lett.* 337 (2023). <https://doi.org/10.1016/j.matlet.2023.133930>.
- [33] C. Manière, T. Grippi, S. Marinel, Estimate microstructure development from sintering

- shrinkage: A kinetic field approach, *Mater. Today Commun.* 31 (2022) 1–29. <https://doi.org/10.1016/j.mtcomm.2022.103269>.
- [34] C. Manière, J.S. Diatta, C. Couder, C. Harnois, S. Marinel, Spark plasma sintering grain growth assessment by densification kinetics analysis, *Scr. Mater.* 228 (2023). <https://doi.org/10.1016/j.scriptamat.2023.115346>.
- [35] C. Manière, L. Durand, E. Brisson, H. Desplats, P. Carré, P. Rogeon, C. Estournès, Contact resistances in spark plasma sintering: From in-situ and ex-situ determinations to an extended model for the scale up of the process, *J. Eur. Ceram. Soc.* 37 (2017) 1593–1605. <https://doi.org/10.1016/j.jeurceramsoc.2016.12.010>.
- [36] C. Manière, C. Harnois, G. Riquet, J. Lecourt, C. Bilot, S. Marinel, Flash spark plasma sintering of zirconia nanoparticles: Electro-thermal-mechanical-microstructural simulation and scalability solutions, *J. Eur. Ceram. Soc.* 42 (2022) 216–226. <https://doi.org/10.1016/j.jeurceramsoc.2021.09.021>.
- [37] J. Le Cloarec, S. Marinel, G. Chevallier, C. Estournès, C. Manière, Impact of graphite foil rolling on the thermal field homogeneity of spark plasma sintering, *Ceram. Int.* 49 (2023) 19545–19551. <https://doi.org/10.1016/j.ceramint.2023.03.028>.
- [38] G. Lee, C. Manière, J. McKittrick, E.A. Olevsky, Electric current effects in spark plasma sintering: From the evidence of physical phenomenon to constitutive equation formulation, *Scr. Mater.* 170 (2019) 90–94. <https://doi.org/10.1016/j.scriptamat.2019.05.040>.
- [39] G. Lee, E.A. Olevsky, C. Manière, A. Maximenko, O. Izhvanov, C. Back, J. McKittrick, Effect of electric current on densification behavior of conductive ceramic powders consolidated by spark plasma sintering, *Acta Mater.* 144 (2018) 524–533. <https://doi.org/10.1016/j.actamat.2017.11.010>.
- [40] U. Kus, PhD, Etude De La Contribution De La Technique Spark Plasma Sintering a L’Optimisation Des Propriétés Mécaniques De L’Alliage De Titane TA6V, Université Toulouse III Paul-Sabatier, 2017.
- [41] M.J. Donachie, *Titanium: A technical guide*, 2000.
- [42] M. Cesbron, Analyse des microstructures et étude du comportement mécanique de pièces en alliage de Ti-6Al-4V issues d’un procédé de fabrication de poudre métallique., 2020.
- [43] N. Milošević, I. Aleksic, Thermophysical properties of solid phase Ti-6Al-4V alloy over a wide temperature range, *Int. J. Mater. Res.* 104 (2013) 462–470. <https://doi.org/10.3139/146.110889>.
- [44] Q. Yan, B. Chen, N. Kang, X. Lin, S. Lv, K. Kondoh, S. Li, J.S. Li, Comparison study on microstructure and mechanical properties of Ti-6Al-4V alloys fabricated by powder-based selective-laser-melting and sintering methods, *Mater. Charact.* 164 (2020). <https://doi.org/10.1016/j.matchar.2020.110358>.
- [45] O.O. Ayodele, M.A. Awotunde, M.B. Shongwe, B.A. Obadele, B.J. Babalola, P.A. Olubambi, Densification and microstructures of hybrid sintering of titanium alloy, *Mater. Today Proc.* 28 (2019) 781–784. <https://doi.org/10.1016/j.matpr.2019.12.297>.
- [46] N. Singh, R. Ummethala, P.S. Karamched, R. Sokkalingam, V. Gopal, G. Manivasagam, K.G. Prashanth, Spark plasma sintering of Ti6Al4V metal matrix composites: Microstructure, mechanical and corrosion properties, *J. Alloys Compd.* 865 (2021) 158875. <https://doi.org/10.1016/j.jallcom.2021.158875>.
- [47] Y. Xue, L.H. Lang, G.L. Bu, L. Li, Densification modeling of titanium alloy powder during hot isostatic pressing, *Sci. Sinter.* 43 (2011) 247–260. <https://doi.org/10.2298/SOS1103247X>.
- [48] L. Badea, M. Surand, J. Ruau, B. Viguier, Creep behavior of Ti-6Al-4V from 450°C TO 600°C, *UPB Sci. Bull. Ser. B Chem. Mater. Sci.* 76 (2014) 185–196.
- [49] C. Manière, L. Durand, C. Estournès, Powder/die friction in the spark plasma sintering process: Modelling and experimental identification, *Scr. Mater.* 116 (2016) 139–142. <https://doi.org/10.1016/j.scriptamat.2016.01.040>.